*photonics*

MDPI

*Article*

# Research on Polarization Phase Diversity Method for Cophase Errors and Polarization Aberrations in Sparse Aperture Optical Systems

**Xiyu Liu [1,2,3], Xin Zhang [1,*], Junliu Fan [2], Baohua Chen [2] and An Xu [1,2,4]**

[1] Suzhou Institute of Biomedical Engineering and Technology, Chinese Academy of Sciences, Suzhou 215163, China; 2311111013@post.usts.edu.cn (X.L.); 2311111018@post.usts.edu.cn (A.X.)
[2] Key Laboratory of Efficient Low-Carbon Energy Conversion and Utilization of Jiangsu Provincial Higher Education Institutions, Suzhou University of Science and Technology, Suzhou 215009, China; fanjunliu@usts.edu.cn (J.F.); chenbaohua@mail.usts.edu.cn (B.C.)
[3] Graduate Workstation in Suzhou FOIF Co., Ltd., Suzhou 215006, China
[4] Graduate Workstation in Suzhou Zhangjiagang Optical Instrument Co., Ltd., Suzhou 215616, China
* Correspondence: zhangx@sibet.ac.cn

**Abstract**

Sparse aperture optical systems employ separated subapertures to achieve equivalent large aperture high resolution imaging, but they are also more susceptible to the combined effects of cophase errors and polarization aberrations, which lead to point spread function distortion and image quality degradation. To address this problem, this paper proposes a Polarization Phase Diversity (PPD) method for cophase errors and polarization aberrations in sparse aperture optical systems. Based on the Jones pupil theory, a unified imaging model incorporating both cophase errors and polarization aberrations is established. By combining focused and defocused images acquired under different analyzer directions, a polarization multichannel observation framework is constructed to jointly retrieve piston, tilt, diattenuation, and retardance parameters. Numerical simulations are mainly carried out on a Golay3 sparse aperture optical system, and additional Gaussian-noise and Golay6 simulations are performed to evaluate the robustness and extensibility of the proposed framework. The results show that, except for the phase-equivalent ambiguity of the piston term, the proposed method can accurately recover the cophase and polarization-aberration parameters under noise-free conditions. Compared with conventional methods considering only cophase errors, the proposed method achieves better image restoration performance in terms of image sharpness, detail recovery, PSNR, and SSIM. The noise experiments further demonstrate that the full-parameter restoration maintains clear advantages under noisy observations, and the Golay6 results indicate that the framework can be extended to sparse aperture configurations with more subapertures. The proposed method provides an effective approach for error sensing and image restoration in sparse aperture optical systems.

**Keywords:** sparse aperture optical system; PPD; cophase error; polarization aberration

Check for updates

Received: 7 May 2026
Revised: 1 June 2026
Accepted: 5 June 2026
Published: 11 June 2026

**Copyright:** © 2026 by the authors. Licensee MDPI, Basel, Switzerland. This article is an open access article distributed under the terms and conditions of the Creative Commons Attribution (CC BY) license.

## 1. Introduction

In the fields of astronomical observation and remote sensing, improving the spatial resolution of optical imaging systems usually requires increasing the system aperture. However, a larger aperture also increases the difficulties of optical fabrication, alignment, testing, and structural support, thereby significantly raising the overall system cost. Sparse

aperture optical systems provide a potential route to synthesize large-equivalent-aperture resolution by arranging multiple separated subapertures, thereby reducing the fabrication, structural support, and deployment burdens associated with monolithic large-aperture systems. However, their practical imaging performance does not automatically surpass that of conventional full-aperture systems; instead, it strongly depends on pupil configuration, co-phasing accuracy, polarization effects, and subsequent computational restoration [1,2].

Nevertheless, because sparse aperture systems are composed of multiple physically separate subapertures, they are more sensitive to alignment errors and structural disturbances than conventional full aperture systems. In practical applications, cophase errors are inevitably introduced into the subapertures, mainly in the form of piston and tilt errors. These errors prevent the wavefronts from different subapertures from being coherently superimposed on the image plane, resulting in point spread function (PSF) distortion and degradation of image quality. To solve this problem, phase diversity has been widely studied as an image based wavefront sensing technique and has shown effectiveness in aberration retrieval, segmented-aperture phasing, and related inverse imaging problems [3–6].

In addition to cophase errors, polarization aberrations induced by polarization dependent effects cannot be neglected in high precision optical imaging systems. Since the reflection and transmission characteristics of optical surfaces vary with polarization state, different polarization components undergo different amplitude attenuation and phase delay during propagation, giving rise to diattenuation and retardance. These polarization aberrations may further reduce image contrast and restoration quality, especially in systems with multiple reflective surfaces, off-axis configurations, or complex pupil structures [7,8].

Recent studies have shown that polarization effects in sparse aperture optical systems deserve particular attention. Research on the polarization characteristics of sparse aperture systems has indicated that polarization aberrations are closely related to the subaperture arrangement and can introduce additional image degradation [9]. Meanwhile, polarization information has also been introduced into sparse aperture image enhancement and fusion, demonstrating its effectiveness in compensating for information loss and improving texture details and contrast [10]. However, most existing phase diversity methods are still based on scalar diffraction theory and mainly focus on scalar wavefront aberration sensing. For sparse aperture optical systems with polarization effects, cophase errors and polarization aberrations are coupled in the imaging process. If only scalar cophase errors are estimated while polarization aberrations are ignored, the imaging model becomes physically incomplete, which in turn limits inversion accuracy and restoration performance.

Motivated by these issues, this paper investigates a phase diversity based joint inversion method for cophase errors and polarization aberrations in sparse aperture optical systems. Based on the Jones pupil model, a unified imaging model incorporating both cophase errors and polarization parameters is established. By combining multichannel polarization observations with focused and defocused images, the proposed method enables simultaneous retrieval of cophase error parameters and polarization aberration parameters, thereby providing theoretical support for accurate error sensing and high quality image restoration in sparse aperture optical systems.

The novelty of this work lies in extending the conventional phase diversity framework from scalar cophase-error retrieval to a polarization multichannel joint inversion problem in sparse aperture optical systems. Specifically, focused and defocused observations under two analyzer directions are combined to construct a four-channel Polarization Phase Diversity framework, in which piston, tilt, diattenuation, and retardance parameters are retrieved simultaneously within a unified optimization process. In addition, a joint objective function is formulated by combining multichannel least-squares fitting with a leave-one-out cross-validation term, so that the common object spectrum can be eliminated

while the consistency of parameter estimation among different observation channels is enhanced. Numerical simulations are then performed to evaluate the parameter-retrieval accuracy and image-restoration performance of the proposed method under different degradation conditions.

## 2. Basic Principles

### *2.1. Basic Theory of Polarized Sparse Aperture*

A sparse aperture optical system replaces a conventional monolithic large aperture structure through the combination of multiple smaller subapertures in a non-redundant pupil configuration. By exploiting the coherent superposition effect among the subapertures, it can achieve a resolution close to that of a large aperture telescope while maintaining a lightweight structure. According to Fourier optics theory, such a system can be approximately regarded as a linear and shift-invariant system. On this basis, the overall pupil function of the system can be expressed as the sum of the transmission functions of all subapertures. For an array composed of subapertures, its pupil function can be written as,

$$\mathrm{P}(x,y) = \sum_{n=1}^{N} A_n(x,y) \cdot \exp\left(j\frac{2\pi}{\lambda} W_n(x,y)\right). \tag{1}$$

Here, $(x,y)$ denotes the pupil plane coordinates, $A_n(x,y)$ is the binary aperture function of the $n$-th subaperture, $\lambda$ is the wavelength, and $W_n(x,y)$ denotes the wave aberration associated with the $n$-th subaperture.

In precision optical systems that aim for extremely high imaging quality, polarization effects induced by optical thin films and large angle reflections cannot be neglected in addition to the scalar wave aberrations described above. When light is reflected from or transmitted through metallic or dielectric film surfaces, the amplitude attenuation and phase variation of its s-polarized and p-polarized components are generally different. This difference can be described by the Fresnel equations and ultimately leads to a change in the polarization state of the emerging light [11]. In imaging systems, such polarization dependent amplitude and phase modulation is collectively referred to as polarization aberration. To describe scalar wavefront errors and vector polarization effects within a unified framework, the scalar pupil function is extended to a more general Jones pupil. The Jones pupil is a $2 \times 2$ complex matrix valued function, each element of which corresponds to the complex amplitude transfer function of a particular polarization component. When both cophase errors and polarization aberrations are present in the system, the pupil function should be described in the form of a $2 \times 2$ Jones matrix:

$$\mathbf{P}(x,y) = \sum_{n=1}^{N} \mathrm{circ}\left(\frac{\sqrt{(x-x_n)^2+(y-y_n)^2}}{\mathrm{D}/2}\right) \cdot \exp[i2\pi W_n(\rho_n,\phi_n)] \cdot \mathbf{J}_n(\rho_n,\phi_n). \tag{2}$$

Here, $\mathrm{circ}(\cdot)$ denotes the circular aperture function, D is the diameter of the subaperture, $(x_n, y_n)$ denotes the center coordinates of the $n$-th subaperture, $W_n(\rho_n,\phi_n)$ represents the scalar wave aberration caused by cophase errors, and $\mathbf{J}_n(\rho_n,\phi_n)$ denotes the Jones matrix describing polarization aberration. The normalized radial coordinate $\rho_n$ and angular coordinate $\phi_n$ are defined as follows:

$$\rho_n = \frac{2\sqrt{(x-x_n)^2+(y-y_n)^2}}{d},\ \phi_n = \arctan\left(\frac{y-y_n}{x-x_n}\right). \tag{3}$$

To enable quantitative inversion of the parameters, both the scalar wave aberration and the polarization aberration need to be parameterized. For cophase errors, this study mainly considers the low order components that have the most significant influence on imaging quality, namely piston error and tilt error. Consistent with the implementation in this work, the wave aberration is expanded using low order Zernike polynomials, and the cophase error of the $n$-th subaperture can be expressed as

$$W_n(\rho_n, \phi_n) = w_0^{(n)} + w_{1x}^{(n)} \cdot 2\rho_n \cos\phi_n + w_{1y}^{(n)} \cdot 2\rho_n \sin\phi_n. \tag{4}$$

Here, $w_0^{(n)}$ denotes the piston error, while $w_{1x}^{(n)}$ and $w_{1y}^{(n)}$ denote the tilt errors in the $x$ and $y$ directions, respectively, both expressed in waves.

The essence of polarization aberration lies in the different responses of the system to orthogonal polarization eigenstates. This difference can be characterized by two physical quantities, namely diattenuation and retardance. Diattenuation describes the difference in transmittance or reflectance of the system for two orthogonal polarization components, whereas retardance describes the phase difference between these two components. For systems composed of thin films or mirrors, polarization aberrations are usually spatially varying, i.e., their distributions over the pupil plane are not uniform. To effectively characterize this spatial variation, only the constant term and the first-order terms in the $x$ and $y$ directions are retained for both diattenuation and retardance within each subaperture, consistent with the implementation adopted in this work. The polarization aberration Jones matrix of the $n$-th subaperture can then be written as

$$\mathbf{J}_n(\rho_n, \phi_n) = \begin{bmatrix} e^{-\frac{d_n(\rho_n,\phi_n)}{2}} \cos\frac{\Delta_n(\rho_n,\phi_n)}{2} & -i\sin\frac{\Delta_n(\rho_n,\phi_n)}{2} \\ i\sin\frac{\Delta_n(\rho_n,\phi_n)}{2} & e^{\frac{d_n(\rho_n,\phi_n)}{2}} \cos\frac{\Delta_n(\rho_n,\phi_n)}{2} \end{bmatrix}. \tag{5}$$

Here, the diattenuation $d_n$ and the retardance $\Delta_n$ are likewise expanded using low order Zernike polynomials:

$$d_n(\rho_n, \phi_n) = d_0^{(n)} + d_{1x}^{(n)} \cdot 2\rho_n \cos\phi_n + d_{1y}^{(n)} \cdot 2\rho_n \sin\phi_n \tag{6}$$

$$\Delta_n(\rho_n, \phi_n) = 2\pi\left[\Delta_0^{(n)} + \Delta_{1x}^{(n)} \cdot 2\rho_n \cos\phi_n + \Delta_{1y}^{(n)} \cdot 2\rho_n \sin\phi_n\right]. \tag{7}$$

Here, $d_0^{(n)}$, $d_{1x}^{(n)}$, and $d_{1y}^{(n)}$ are the constant term and the gradient terms in the $x$ and $y$ directions of the diattenuation, respectively, and are dimensionless; $\Delta_0^{(n)}$, $\Delta_{1x}^{(n)}$, and $\Delta_{1y}^{(n)}$ are the constant term and the gradient terms in the $x$ and $y$ directions of the retardance, respectively, and are expressed in waves. In the actual calculation, $\Delta_n(\rho_n, \phi_n)$ is first multiplied by $2\pi$ and converted into radians before being substituted into the Jones matrix.

### *2.2. Polarization Phase Diversity Method for Aberration Parameters Based on Polarization Multichannel Observation*

Phase diversity is an image based wavefront sensing method whose basic idea is to introduce a known phase perturbation during the imaging process to improve the identifiability of system aberration parameters. For an incoherent imaging system, the focused and defocused images in the frequency domain can be expressed as

$$G_f(u, v) = \mathrm{F}(u, v)H_f(u, v), \quad G_d(u, v) = \mathrm{F}(u, v)H_d(u, v). \tag{8}$$

where $F(u, v)$ denotes the object spectrum, $G(u, v)$ denotes the spectrum of the observed image, and $H(u, v)$ denotes the optical transfer function.

In conventional phase diversity, since the object spectrum $F(u,v)$ is unknown, it is usually eliminated by constructing a loss function, thereby transforming the wavefront sensing problem into a nonlinear optimization problem with respect to the aberration parameter vector $\theta$. Under the assumption of additive white Gaussian noise, the loss function of the classical two image phase diversity method can be written as

$$L(\theta) = \sum_{u,v} \frac{| G_f H_d - G_d H_f |^2}{| H_f |^2 + | H_d |^2}. \tag{9}$$

To achieve joint detection of polarization aberrations, we extend the observations by introducing the polarization dimension on the basis of conventional phase diversity. In the simulation, 45° linearly polarized light is used for illumination, and 0° and 90° linear polarizers are placed in front of the detector. Images are then acquired at both the focused and defocused planes. As a result, four observed images are obtained in total, namely P0-F, P0-D, P90-F, and P90-D, indexed by $k = 1, 2, 3, 4$.

Under the assumption that the target is a unpolarized intensity object, or that its polarization response can be neglected, the four channels share the same object spectrum $F(u,v)$, and the differences between the channels are only reflected in the system transfer function $H_k(u,v;\theta)$. Therefore, the four channel frequency domain imaging model can be uniformly written as

$$G_k(u,v) = F(u,v)H_k(u,v;\theta), k = 1, 2, 3, 4. \tag{10}$$

Based on this, a four channel joint least squares loss function is constructed as

$$L_{LS}(\theta) = \sum_{u,v\in\Omega} \sum_{k=1}^{4} |G_k(u,v) - F(u,v)H_k(u,v;\theta)|^2. \tag{11}$$

By eliminating the unknown object spectrum, its optimal estimate can be obtained as

$$\hat{F}(u,v) = \frac{\sum_{k=1}^{4} G_k(u,v)H_k^*(u,v;\theta)}{\sum_{k=1}^{4} \left| H_k(u,v;\theta) \right|^2 + \varepsilon}. \tag{12}$$

where $\varepsilon$ is a numerical stabilization term. Substituting this estimate back into the loss function yields a least squares objective function depending only on the aberration parameter vector $\theta$.

To further improve the robustness of the inversion against noise and channel errors, a leave-one-out and cross-validation loss is introduced in addition to the least squares loss. In each round, one image is left out as validation data, while the other three images are used to estimate the object spectrum; the estimated spectrum is then used to predict the left out image, and the residual is calculated. When the $k$-th image is left out, the estimate of the object spectrum is

$$\hat{F}^{(k)}(u,v) = \frac{\sum_{j\neq k} G_j(u,v)H_j^*(u,v;\theta)}{\sum_{j\neq k} \left| H_j(u,v;\theta) \right|^2 + \varepsilon}. \tag{13}$$

and the corresponding prediction error is

$$E_k = \sum_{u,v\in\Omega} \left| G_k(u,v) - \hat{F}^{(k)}(u,v)H_k(u,v;\theta) \right|^2. \tag{14}$$

Averaging over the four leave-one-out cases gives the cross-validation loss

$$L_{CV}(\theta) = \frac{1}{4}\sum_{k=1}^{4} E_k. \tag{15}$$

Finally, we adopt a weighted combination of the least squares loss and the cross-validation loss as the objective function for aberration parameter inversion:

$$L(\theta) = \lambda_1 L_{LS}(\theta) + \lambda_2 L_{CV}(\theta) \tag{16}$$

Here, $\lambda_1$ and $\lambda_2$ are the weighting coefficients of the multichannel least-squares loss and the leave-one-out cross-validation loss, respectively. In this work, $\lambda_1 = \lambda_2 = 1$ is adopted. This setting is used because $L_{\mathrm{LS}}$ and $L_{\mathrm{CV}}$ are both constructed from squared Fourier-domain residuals of the same four-channel imaging model and therefore have the same physical dimension. Equal weighting gives the direct fitting residual and the leave-one-out channel-prediction residual the same priority, without introducing an additional empirical preference between the two terms, As shown in Figure 1.

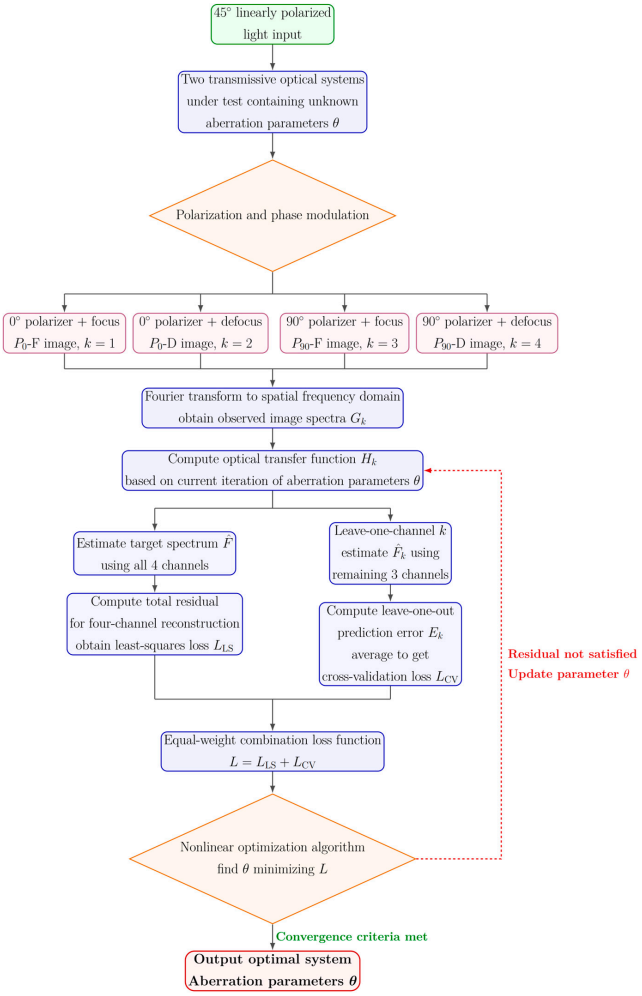



**Figure 1.** Flowchart of the joint inversion of aberration parameters based on polarization multichannel observations. Green boxes denote the input illumination and final convergence/output, blue rectangles denote calculation and optimization operations, orange diamonds denote modulation or convergence-judgment steps, and pink boxes denote the generated observation channels or output parameters. The red dashed arrow indicates the iterative feedback loop in which the aberration parameter vector is updated until the residual criterion is satisfied.

## 3. Simulation Design and Results Analysis

### *3.1. Simulation Conditions and Parameter Settings*

The main numerical simulations in this study are carried out using a Golay3 sparse aperture optical system, and an additional Golay6 configuration is further introduced to evaluate the extensibility of the proposed framework. The Golay3 configuration consists of three identical circular subapertures, and its arrangement provides favorable Fourier coverage characteristics and high imaging resolution.

Figure 2 illustrates the closed-loop simulation framework for wavefront sensing and image restoration of a sparse aperture optical system based on the Jones pupil model. First, a Jones pupil model is constructed according to the initialized optical system configuration, and random aberration parameters are generated to simulate system errors in a non-ideal imaging environment. On this basis, degraded simulated images containing both cophase errors and polarization aberrations are produced through the forward imaging process. Subsequently, a loss function is formulated using the phase diversity method, and the model parameters are iteratively updated using an optimization algorithm until the loss satisfies a prescribed convergence criterion or the maximum number of iterations is reached, thereby yielding estimates of the cophase error parameters and polarization aberration parameters. Finally, the optical transfer functions corresponding to each observation channel are reconstructed from the retrieved parameters, and the four degraded observed images are deconvolved separately to verify the accuracy of parameter inversion and to further improve the final imaging quality of the system.

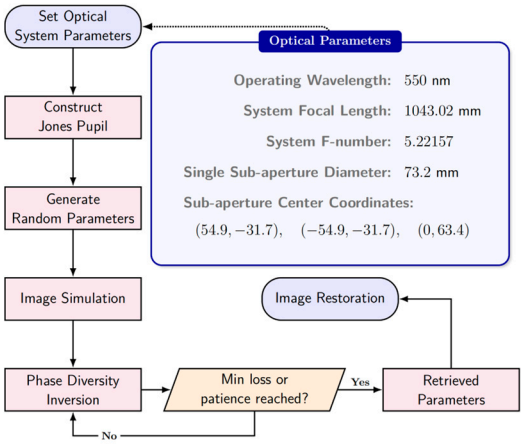



**Figure 2.** Flowchart of simulation for parameter inversion. The light purple rounded boxes denote the initial optical-system settings and image-restoration module, the light pink rectangles denote the Jones-pupil construction, random-parameter generation, image-simulation, phase-diversity inversion, and retrieved-parameter modules, the beige parallelogram denotes the convergence-judgment condition, and the blue-outlined box summarizes the optical parameters used in the simulation. The arrows indicate the forward simulation, inversion, restoration, and feedback workflow.

For the implementation of phase diversity, both focused and defocused images are required. In this work, the defocus distance is set to $1\lambda$. The defocus distance affects the diversity between the focused and defocused images and therefore influences parameter observability. If the defocus is too small, the two images provide insufficiently independent information, making the inverse problem less sensitive to aberration parameters. If the defocus is too large, high-frequency information may be excessively attenuated, which can increase the ill-posedness of restoration and parameter inversion. In this study, $1\lambda$ was adopted as a practical and commonly used defocus setting, which provides sufficient phase diversity while keeping the defocused image degradation within a controllable range.

According to the parameterized model established above, the unknown parameters to be estimated include the cophase error parameters and the polarization aberration parameters of each subaperture. Specifically, the cophase error parameters consist of the piston error $w_0^n$, the tilt error in the $x$ direction $w_{1x}^n$, and the tilt error in the $y$ direction $w_{1y}^n$ for each subaperture. The polarization aberration parameters include the diattenuation parameters $d_0^n$, $d_{1x}^n$, and $d_{1y}^n$, as well as the retardance parameters $\Delta_0^n$, $\Delta_{1x}^n$, and $\Delta_{1y}^n$.

In the simulations, the cophase error parameters are randomly initialized within the range $[-1\lambda, 1\lambda]$. The diattenuation coefficients d are randomly initialized within $[-0.2, 0.2]$, whereas the retardance coefficients $\Delta$ are randomly initialized within $[-0.2\lambda, 0.2\lambda]$. The cophase-error interval is selected to cover one wavelength of piston variation and the corresponding low-order tilt perturbations considered in sparse-aperture phasing. The diattenuation and retardance intervals define the low-order polarization-aberration perturbation range adopted in this study. These bounds are not used to suppress the contribution of polarization aberrations, but to keep the initialization and projected optimization within the same modeled parameter domain.

The Adam (Adaptive Moment Estimation) optimizer is employed to minimize the loss function [12]. Since the variables to be optimized simultaneously include both cophase error parameters and polarization aberration parameters, and the joint loss function is highly nonlinear, the Adam algorithm is beneficial for the convergence stability and computational efficiency of the multiparameter joint inversion process.

To obtain more accurate parameter estimates in the later stage of optimization, a ReduceLROnPlateau learning-rate scheduling strategy is adopted based on the PyTorch2.4.1 optimization framework [13]. When the loss does not exhibit a significant decrease over $P$ consecutive iterations, the current learning rate is reduced by a factor of $\gamma$. In this work, the decay factor is set to $\gamma = 0.5$, the patience parameter to $P = 2000$, the improvement threshold to $\delta = 10^{-15}$, and the minimum learning rate to $10^{-10}$.

To prevent gradient explosion from destabilizing the optimization process, gradient clipping is applied to the parameter gradients at each iteration, with the maximum gradient norm set to 0.1 [14].

Because cophase errors in sparse aperture systems exhibit global piston and global tilt degeneracies, a reference constraint must be introduced during optimization. In this work, the piston error $w_0^1$ and the tilt errors $w_{1x}^1$ and $w_{1y}^1$ of the first subaperture are fixed at zero as the reference baseline. It should be noted that this reference constraint is imposed only on the cophase error parameters. Under the present modeling and observation configuration, the polarization aberration parameters do not exhibit the same global piston or global tilt degeneracy as the cophase error terms, and are therefore estimated for all subapertures.

In addition, to ensure the physical plausibility of the estimated parameters, boundary constraints are imposed after each parameter update during optimization, using the same ranges as those adopted for parameter initialization, i.e.,

$$\begin{cases} w_0^{(n)}, w_{1x}^{(n)}, w_{1y}^{(n)} \in [-1.0, 1.0], \ n = 2, 3, \\ d_0^{(n)}, d_{1x}^{(n)}, d_{1y}^{(n)}, \Delta_0^{(n)}, \Delta_{1x}^{(n)}, \Delta_{1y}^{(n)} \in [-0.2, 0.2], \ n = 1, 2, 3. \end{cases} \tag{17}$$

### *3.2. Simulation Results and Robustness Analysis Under the Golay3 Configuration*

In this section, simulation experiments are conducted under the Golay3 sparse aperture configuration to evaluate the parameter inversion accuracy, image restoration performance, and noise robustness of the proposed method. The classical Cameraman image is used as the target, and the optical system parameters are kept the same as those in Section 3.1. First, the noise-free case is analyzed as a baseline to verify the correctness and stability of parameter inversion. The input images used for inversion are shown in Figure 3.



(**a**) (**b**) (**c**) (**d**)

**Figure 3.** Four-channel degraded images used for parameter inversion under the Golay3 configuration: (**a**) P0-F, (**b**) P0-D, (**c**) P90-F, and (**d**) P90-D. P0 and P90 denote the 0° and 90° analyzer directions, respectively, while F and D denote the focused and defocused imaging planes.

First, parameter inversion is performed under noise free conditions, and the estimated results of all parameters are obtained, as shown in Table 1.

**Table 1.** Inversion results of all parameters under noise free conditions.

| Subaperture | Parameter Name | Ground Truth Value | Estimated Value | Absolute Error | Relative Error (%) |
|---|---|---|---|---|---|
| 1 | $\omega_0$ | 0 | 0 | $0.000000 \times 10^{+0}$ | 0.00 |
| 1 | $\omega_{1x}$ | 0 | 0 | $0.000000 \times 10^{+0}$ | 0.00 |
| 1 | $\omega_{1y}$ | 0 | 0 | $0.000000 \times 10^{+0}$ | 0.00 |
| 1 | $d_0$ | 0.09767 | 0.09767 | $1.346791 \times 10^{-7}$ | 0.00 |
| 1 | $d_{1x}$ | −0.013993 | −0.013994 | $7.455310 \times 10^{-8}$ | 0.00 |
| 1 | $d_{1y}$ | 0.190143 | 0.190143 | $3.383016 \times 10^{-8}$ | 0.00 |
| 1 | $\Delta_0$ | −0.027041 | −0.027041 | $9.778861 \times 10^{-8}$ | 0.00 |
| 1 | $\Delta_{1x}$ | −0.179043 | −0.179043 | $1.926399 \times 10^{-8}$ | 0.00 |
| 1 | $\Delta_{1y}$ | 0.001699 | 0.001699 | $6.384240 \times 10^{-8}$ | 0.00 |
| 2 | $w_0$ | −0.631096 | −0.631096 | $1.116978 \times 10^{-7}$ | 0.00 |
| 2 | $w_{1x}$ | −0.941474 | −0.941474 | $2.700285 \times 10^{-8}$ | 0.00 |
| 2 | $w_{1y}$ | 0.439433 | 0.439433 | $1.146314 \times 10^{-7}$ | 0.00 |
| 2 | $d_0$ | −0.143295 | −0.143295 | $2.805162 \times 10^{-7}$ | 0.00 |
| 2 | $d_{1x}$ | 0.106805 | 0.106805 | $2.101661 \times 10^{-9}$ | 0.00 |
| 2 | $d_{1y}$ | 0.138624 | 0.138624 | $1.117721 \times 10^{-7}$ | 0.00 |
| 2 | $\Delta_0$ | 0.073753 | 0.073753 | $4.934321 \times 10^{-7}$ | 0.00 |
| 2 | $\Delta_{1x}$ | 0.018724 | 0.018724 | $7.941595 \times 10^{-8}$ | 0.00 |
| 2 | $\Delta_{1y}$ | 0.105219 | 0.105219 | $2.302150 \times 10^{-8}$ | 0.00 |
| 3 | $w_0$ | 0.462507 | −0.537493 | $1.000000 \times 10^{+0}$ | 216.21 |
| 3 | $w_{1x}$ | −0.271372 | −0.271372 | $5.652321 \times 10^{-8}$ | 0.00 |
| 3 | $w_{1y}$ | −0.9957 | −0.9957 | $5.663841 \times 10^{-8}$ | 0.00 |
| 3 | $d_0$ | 0.163424 | 0.163424 | $6.035645 \times 10^{-8}$ | 0.00 |
| 3 | $d_{1x}$ | 0.073121 | 0.073121 | $8.004195 \times 10^{-8}$ | 0.00 |
| 3 | $d_{1y}$ | −0.040298 | −0.040298 | $4.406233 \times 10^{-7}$ | 0.00 |
| 3 | $\Delta_0$ | 0.057266 | 0.057266 | $2.739612 \times 10^{-7}$ | 0.00 |
| 3 | $\Delta_{1x}$ | 0.168776 | 0.168776 | $1.989560 \times 10^{-8}$ | 0.00 |
| 3 | $\Delta_{1y}$ | −0.181687 | −0.181688 | $1.546430 \times 10^{-7}$ | 0.00 |

Under noise free conditions, the table presents the inversion results of the cophase error parameters and polarization aberration parameters for the three subapertures. Overall, except for the piston term, the estimated values of all parameters are in excellent agreement with the true values. Their absolute errors are mainly on the order of $1 \times 10^{-7}$, and the relative errors are almost negligible, indicating that the proposed method possesses extremely high inversion accuracy and good numerical stability under ideal conditions. These results further demonstrate that, during the multiparameter joint inversion process, no significant parameter coupling or mixing occurs between the cophase error terms and

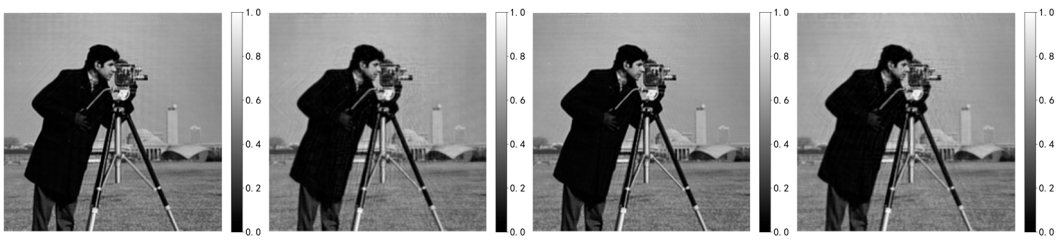
the polarization aberration terms, and that the algorithm is able to effectively distinguish and accurately recover error components originating from different physical sources.

For the tilt related parameters, including the wavefront tilt error $w_1$, the diattenuation tilt term $d_1$, and the retardance tilt term $\Delta_1$, high precision inversion with nearly zero relative error is achieved for all subapertures. This indicates that the proposed method is highly sensitive to spatial gradient type errors and has good observability, enabling it to stably capture small perturbations introduced by phase slopes and polarization gradients. In contrast, the inversion errors of the constant polarization aberration terms $d_0$ and $\Delta_0$ are slightly larger. Nevertheless, their absolute errors remain extremely small, and their relative errors are all below 1%, indicating that the method still maintains stable performance and strong discriminative capability for both amplitude type and phase type constant errors.

It should be noted that, for Subaperture 3, the estimated value of the piston error term $w_0$ differs from the true value by approximately 1. This phenomenon mainly arises from the $2\pi$-periodic non-uniqueness of the piston term in the imaging model, that is, different piston constants may physically correspond to equivalent phase distributions. Therefore, this discrepancy does not indicate inversion failure, but rather a constant shift caused by phase equivalence. From the imaging point of view, such an equivalent solution does not have any substantial influence on the final imaging quality or system correction performance.

In summary, under noise free conditions, the proposed joint inversion method for cophase errors and polarization aberrations is capable of achieving highly accurate and stable parameter estimation in a multisubaperture scenario. In particular, the inversion performance for tilt type errors and polarization aberration parameters is especially prominent, while the periodicity of the piston term does not affect the imaging result. This verifies the correctness and effectiveness of the proposed method under ideal conditions.

To further validate the effectiveness of the proposed method in image restoration, the degraded observed images under four imaging configurations, namely P0-F, P0-D, P90-F, and P90-D, are processed using a unified restoration framework. Figure 4 shows the restoration results obtained when the system parameters are completely known. These results represent the upper bound of restoration performance achievable under the corresponding imaging configurations and serve as reference baselines for comparison with the subsequent inversion-based results. Figure 5 presents a comparison of the restoration performance produced by different restoration strategies. Specifically, the conventional method performs inversion and restoration using only the cophase error parameters, whereas the method proposed in this paper retrieves all parameters, including both the cophase error parameters and the polarization aberration parameters. When polarization aberrations are present in the system, the comparison between these two restoration strategies in Figure 5 not only shows the restored images, but also presents the residual distributions between the restored images and the ground truth image, thereby providing an intuitive illustration of the differences in the ability of the two strategies to characterize the image degradation process.




(**a**) (**b**) (**c**) (**d**)

**Figure 4.** Image restoration results obtained using the true system parameters under the Golay3 configuration: (**a**) P0-F, (**b**) P0-D, (**c**) P90-F, and (**d**) P90-D.

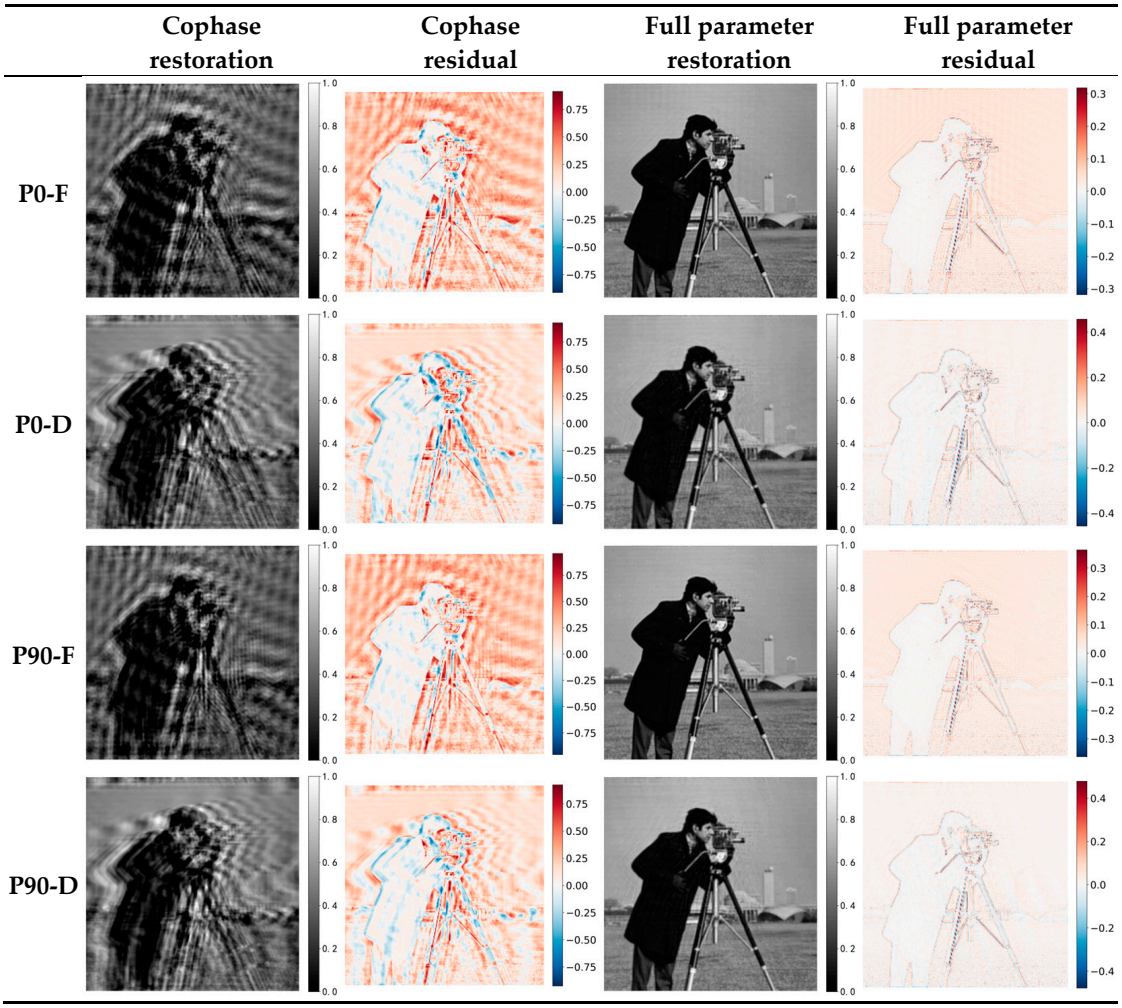



**Figure 5.** Comparison of image restoration and residual results under noise-free conditions. Each row corresponds to one observation channel, and the columns show cophase-only restoration, cophase-only residual, full parameter restoration, and full parameter residual, respectively.

In the comparative image restoration experiments, the visual difference between restoration using only the cophase error parameters and restoration using both the cophase error parameters and the polarization aberration parameters is particularly significant. First, although the restoration method based solely on cophase error parameters can improve the image quality to a certain extent, the overall restored image remains relatively blurred, and the recovery of fine details is still very limited. In particular, in edge contours and regions with complex textures, visible discrepancies can still be observed between the restored image and the ground truth. From the residual maps and their corresponding color bars, it can be seen that the image exhibits strong color fluctuations, red and blue regions are widespread and pronounced. This reveals the existence of large local prediction errors in the model. Especially at the boundaries between the human figure and the background, the residual maps show obvious oscillatory patterns and strong error contrast. This indicates that, because the restoration model ignores the effect of polarization aberrations, the description of the point spread function becomes inaccurate, resulting in significant overestimation or underestimation during the restoration process. Consequently, the restored image shows poor recovery of the original details and unsatisfactory overall image quality.

In contrast, the restoration method proposed, which incorporates both cophase error parameters and polarization aberration parameters, performs significantly better than the

conventional method using only cophase error parameters. Under this full parameter restoration mode, image details and the image sharpness are substantially improved. In particular, the contour edges of distant objects and the reconstruction of fine textures become much clearer and sharper. As observed from the residual maps and the corresponding color bars, the peak residuals of the full parameter restoration are far lower than those of the method based only on cophase error parameters. Moreover, the color transitions in the residual maps are smoother and more natural, and the spatial distribution of the errors is more uniform, with the severe red blue deviations near the edges being largely eliminated. The essential reason for this performance difference is that the introduction of polarization aberration parameters greatly improves the accuracy of image restoration. These parameters are able to capture and compensate for more physical information related to imaging details. In particular, with the aid of polarization information, high frequency details can be restored more effectively, thereby significantly reducing restoration errors and yielding clearer results. By contrast, if only the cophase error parameters are used, the restoration performance is inevitably limited by the incompleteness of the physical model, since the polarization information in the image cannot be effectively decoupled and handled.

The overall comparison in Figure 6 further shows that the restoration method combining polarization aberration parameters and cophase error parameters performs well in multiple evaluation metrics. Whether under focused or defocused conditions, or for original images with different polarization directions, the proposed method is capable of achieving stable and high quality restoration, demonstrating its good robustness under a variety of imaging configurations.

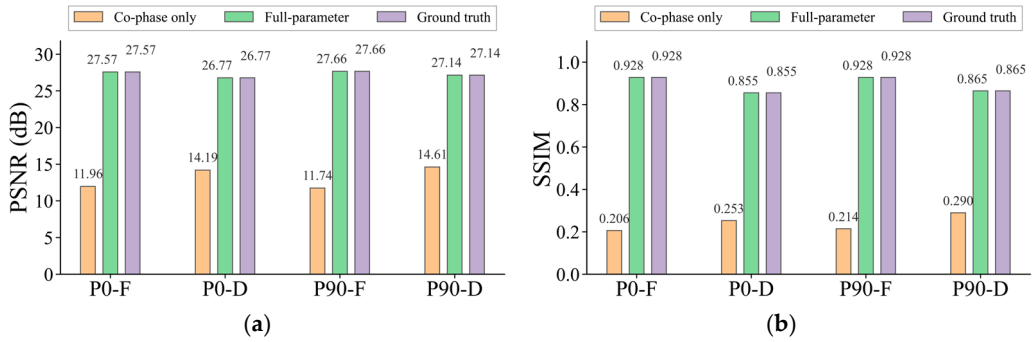



**Figure 6.** Quantitative comparison of image restoration results under noise-free conditions: (**a**) PSNR, (**b**) SSIM.

Under ideal noise free conditions, the conventional Wiener filtering method establishes the imaging degradation model based only on cophase errors. Because it ignores the diattenuation and retardance introduced by the polarization channels, its physical description of the point spread function is incomplete. Experimental results show that this method produces obvious residual blur and artifacts during the restoration process. Quantitative evaluation further indicates that the conventional method yields relatively low performance under all configurations. Under the infocus condition, the PSNR values for the two polarization directions are only 11.96 dB and 11.74 dB, respectively, while the SSIM values remain around 0.21. This indicates that modeling based solely on cophase errors is insufficient for effectively reconstructing the structural information of the image.

In contrast, the proposed Jones inversion method significantly improves the completeness and accuracy of the degradation model by simultaneously incorporating cophase errors and polarization aberrations into the physical modeling. This method more faithfully reproduces the degradation mechanism of the system, leading to substantial improvements in restoration performance under all four imaging configurations. Under the infocus con-

dition, the PSNR values of the two polarization images are improved by 15.61 dB and 15.92 dB, respectively, compared with those of the conventional method, while the SSIM values increase to about 0.93. These results demonstrate that the introduction of polarization aberrations plays a decisive role in improving restoration quality, especially in recovering fine texture details. By comparing the Jones inversion results with the restoration results obtained using the true parameters, a high degree of consistency is observed between them. This further confirms that, in a noise free environment, the performance gain mainly arises from the improved physical completeness of the degradation model rather than from random factors. The experiments fully verify that the Jones inversion method possesses significant modeling advantages and great potential for high quality restoration when dealing with complex imaging degradation.

To further evaluate the robustness of the proposed method under non-ideal imaging conditions, additional experiments were conducted by introducing zero-mean Gaussian noise into the four observed images before parameter inversion. The image intensity was normalized to [0, 1], and the standard deviations of the added Gaussian noise were set to 0.001, 0.002, 0.005, and 0.010, respectively. For each noise level, the aberration parameters were retrieved using the same optimization framework, and the restored images were then obtained using the OTFs reconstructed from the estimated parameters. The corresponding PSNR and SSIM results are shown in Figure 7.

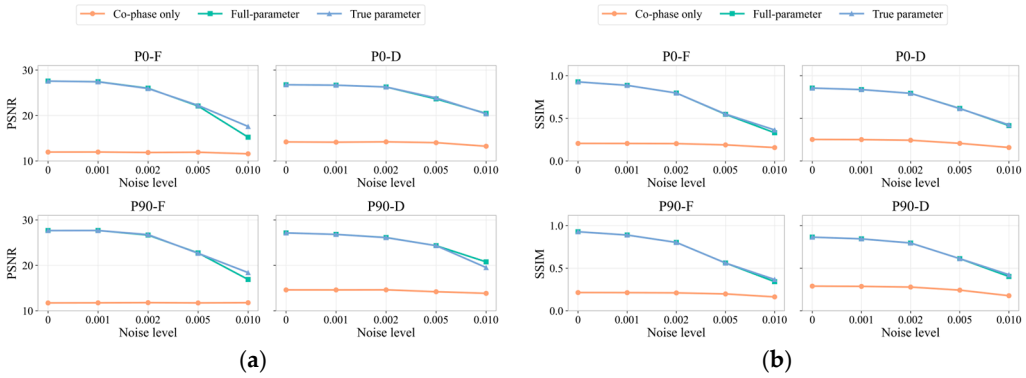



**Figure 7.** Quantitative comparison of image restoration results under different Gaussian noise levels: (**a**) PSNR, (**b**) SSIM.

As shown in Figure 7, both PSNR and SSIM decrease gradually as the noise level increases, indicating that Gaussian noise affects the accuracy of parameter inversion and the subsequent image restoration process. However, the restoration results obtained by the proposed full-parameter method are consistently better than those obtained by the cophase-only method under all tested noise levels. In particular, when the noise standard deviation is relatively low or moderate, the full-parameter restoration results remain close to those obtained using the true parameters. When the noise level further increases to 0.010, the performance gap between the estimated-parameter restoration and the true-parameter restoration becomes more evident, showing that strong noise introduces additional uncertainty into the inversion process. Nevertheless, the proposed method still maintains a clear advantage over the cophase-only model, which demonstrates its robustness and anti-interference capability under noisy observations.

### *3.3. Generalization to the Golay6 Sparse Aperture Configuration*

To further examine the applicability of the proposed framework to sparse aperture configurations with more subapertures, an additional simulation was carried out using a Golay6 sparse aperture configuration. The Golay6 pupil geometry is defined on the pupil plane in millimeters. The six subaperture centers are located at (0.0, −57.8), (50.0, −57.8),

(50.0, 28.9), (25.0, 72.2), (−50.0, 28.9), and (−75.1, −14.4), respectively. Each circular subaperture has a diameter of 47.1 mm and a radius of 23.6 mm. The maximum distance from the pupil origin to a subaperture center is approximately 76.4 mm, giving a circumscribed sparse-aperture pupil radius of approximately 100 mm. Compared with the Golay3 configuration, the number of subapertures increases from three to six, and the number of optimized parameters increases from 24 to 51 because the piston and tilt terms of the first subaperture are fixed as the cophase reference. Except for the pupil geometry, the wavelength, focal length, F-number, pupil sampling size, four-channel observation strategy, parameter ranges, noise settings, and optimization parameters are kept the same as those used in the Golay3 simulations.

Under noise-free conditions, the full-parameter inversion still provides restoration performance very close to that obtained using the true parameters. As shown in Figure 8a,b, the full-parameter and true-parameter bars almost overlap in both PSNR and SSIM for all four observation channels, whereas the cophase-only restoration remains much lower. This trend indicates that the additional degradation introduced by polarization aberrations cannot be adequately compensated by a scalar cophase-only model. Therefore, the performance gain produced by joint cophase-error and polarization-aberration inversion is retained after the pupil is extended from Golay3 to the higher-dimensional Golay6 configuration.

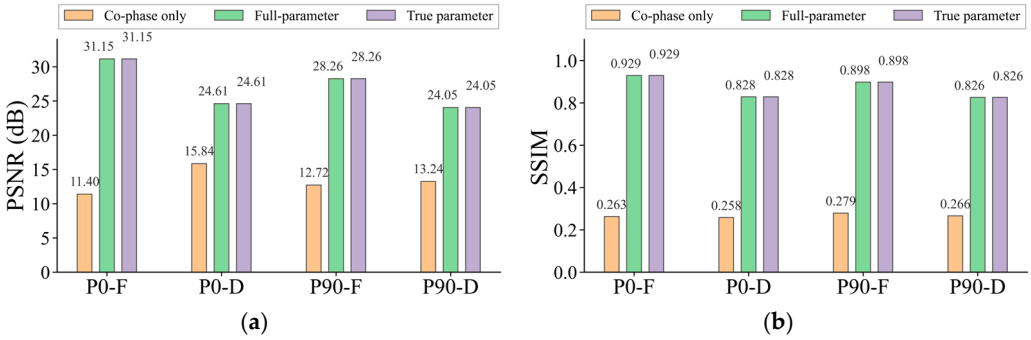



**Figure 8.** Quantitative comparison of Golay6 restoration results under noise-free conditions: (**a**) PSNR, (**b**) SSIM.

The noise robustness of the Golay6 case was further evaluated by adding zero-mean Gaussian noise with the same standard deviations as those used in the Golay3 experiments. The restoration-quality variations with noise are shown in Figure 9. As the noise standard deviation increases, both PSNR and SSIM gradually decrease, and the degradation becomes more evident at the highest noise level. Nevertheless, the full-parameter restoration curves remain close to the true-parameter curves over most noise levels and consistently outperform the cophase-only model, demonstrating the anti-interference capability of the proposed joint inversion framework under the Golay6 pupil configuration.

The computational cost was also evaluated under the same benchmark environment. For the 256 × 256 pupil grid with four observation channels, each optimization iteration is dominated by FFT-based OTF calculation and frequency-domain residual evaluation. The dominant per-iteration complexity can be expressed as $O(KN^2 \log N + KN^2)$, where K is the number of observation channels and N is the one-dimensional pupil sampling size. The measured median runtime increases from $2.521 \times 10^{-2}$ s/iteration for Golay3 to $4.807 \times 10^{-2}$ s/iteration for Golay6, which is consistent with the increased number of subapertures and optimized parameters. In the Golay6 case, convergence is achieved within 13,723–18,982 iterations under the tested noise levels, indicating that the optimization process remains stable when the pupil configuration and parameter dimension are increased.

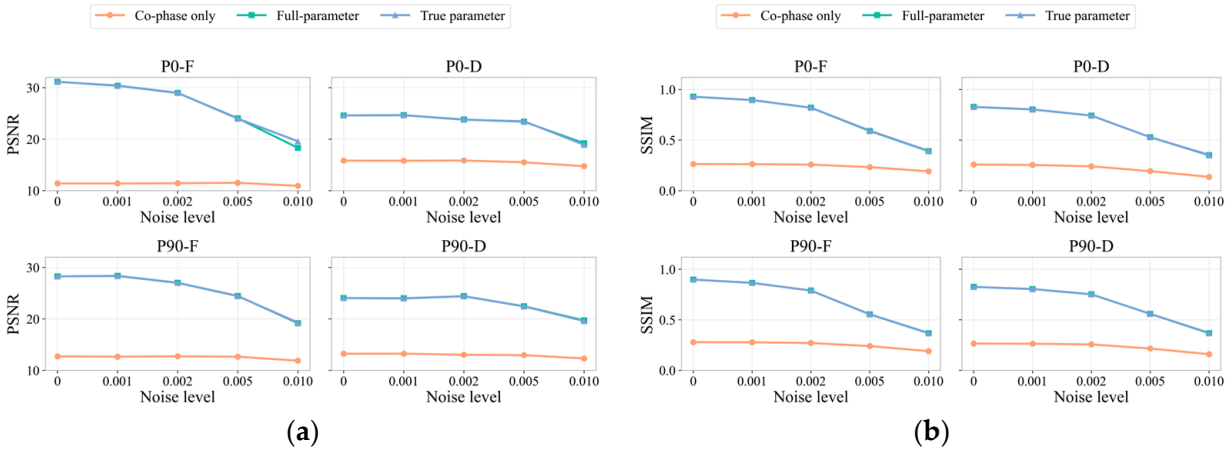



**Figure 9.** Quantitative comparison of Golay6 restoration results under different Gaussian noise levels: (**a**) PSNR, (**b**) SSIM.

It should be noted that, similar to the Golay3 case, the piston terms may still exhibit phase-equivalent solutions differing by an integer number of wavelengths. This periodic ambiguity does not represent a failure of the inversion, because the corresponding point spread functions and restored images remain physically equivalent. Overall, the Golay6 results indicate that the proposed PPD framework is not restricted to the Golay3 example and can be applied to a sparse aperture configuration with more subapertures and a higher-dimensional optimization parameter space.

## 4. Conclusions

In this paper, a Polarization Phase Diversity method for cophase errors and polarization aberrations in sparse aperture optical systems has been investigated based on the Jones pupil model. By introducing piston errors, tilt errors, and polarization aberration parameters including diattenuation and retardance within a unified modeling framework, a physical imaging model incorporating both scalar wavefront aberrations and vector polarization effects has been established. On this basis, a joint inversion framework for multiparameter estimation has been constructed by combining observations from multiple polarization directions as well as focused and defocused planes, and the parameter estimation problem is formulated as a nonlinear optimization problem solved using the Adam algorithm.

Simulation results based on the Golay3 sparse aperture configuration show that the piston term in the cophase error exhibits phase-periodic equivalence in the imaging model, while the proposed method demonstrates high sensitivity and strong discriminative capability for tilt-type spatial gradient errors as well as polarization-aberration parameters. Under noise-free conditions, the proposed method achieves accurate and stable parameter inversion, indicating that the established joint inversion model possesses good numerical stability and parameter observability. Additional Gaussian-noise simulations further show that the proposed full-parameter restoration method maintains better PSNR and SSIM performance than the cophase-only model under noisy observations.

The image restoration experiments further demonstrate that, compared with conventional methods considering only cophase errors, the introduction of polarization aberration modeling provides a more complete description of point spread function degradation and enables a more accurate characterization of the actual imaging degradation process in sparse aperture systems. Based on the full parameter inversion results, the restored images exhibit clear improvements in edge definition, fine texture recovery, and overall sharpness, together with smoother residual distributions and significant gains in objective evaluation

metrics such as PSNR and SSIM. These results indicate that the proposed Polarization Phase Diversity method for cophase errors and polarization aberrations can effectively improve both parameter sensing accuracy and image restoration quality in sparse aperture systems, and can provide useful methodological support for performance analysis and optimization of sparse aperture imaging systems. Furthermore, the Golay6 simulation verifies that the proposed framework can be applied to sparse aperture configurations with more subapertures, indicating its potential applicability beyond the Golay3 configuration.

**Author Contributions:** Conceptualization, X.Z. and A.X.; methodology, X.L. and J.F.; software, X.L.; validation, X.L., J.F. and B.C.; formal analysis, X.L.; investigation, X.L.; resources, X.Z. and A.X.; data curation, X.L. and B.C.; writing—original draft preparation, X.L.; writing—review and editing, X.Z., J.F. and A.X.; visualization, X.L.; supervision, X.Z. and A.X.; project administration, X.Z.; funding acquisition, X.Z. and A.X. All authors have read and agreed to the published version of the manuscript.

**Funding:** The National Natural Science Foundation of China (NSFC) (62275187, 61875145, 11804243); the Jiangsu Province Key Discipline of China's 14th five-year plan (2021135); the Suzhou City Key Laboratory (SZS201202).

**Data Availability Statement:** The original contributions presented in this study are included in the article.

**Conflicts of Interest:** Author Xiyu Liu was employed by the company Graduate Workstation in Suzhou FOIF Co., Ltd. Author An Xu was employed by the company Graduate Workstation in Suzhou Zhangjiagang Optical Instrument Co., Ltd. The remaining authors declare that the research was conducted in the absence of any commercial or financial relationships that could be construed as a potential conflict of interest.

## References

1. Iskender, B.; Oktem, F.S. Image restoration for sparse aperture optical systems. In *Proceedings of the 2018 26th Signal Processing and Communications Applications Conference (SIU)*; IEEE: Piscataway, NJ, USA, 2018; pp. 1–4.
2. Liu, X.; Wang, J.; Wu, Q.; Fan, J.; Chen, B.; Li, Z.; Xu, A. Deep Learning-Based Polarization Image Fusion for Sparse Aperture Optical Systems. *Acta Opt. Sin.* **2025**, *45*, 1510004.
3. Paxman, R.G.; Schulz, T.J.; Fienup, J.R. Joint estimation of object and aberrations by using phase diversity. *J. Opt. Soc. Am. A* **1992**, *9*, 1072–1085. [CrossRef]
4. Zhou, Z.; Zhang, J.; Fu, Q.; Nie, Y. Phase-diversity wavefront sensing enhanced by a Fourier-based neural network. *Opt. Express* **2022**, *30*, 34396–34410. [CrossRef] [PubMed]
5. Zhou, Z.; Zhang, J.; Fu, Q.; Nie, Y. Generalization of learned Fourier-based phase-diversity wavefront sensing. *Opt. Express* **2023**, *31*, 11729–11744. [CrossRef] [PubMed]
6. Luo, F.; Mu, Q.; Peng, Z.; Liu, Y.; Yang, C.; Zhang, X. Poisson phase diversity algorithm with automatic registration for sparse fluorescent images. *Opt. Express* **2025**, *33*, 5877–5889. [CrossRef] [PubMed]
7. Wang, K.; Fu, Q.; Wang, B.; Shi, H.; Liu, J.; Wang, Q.; Wang, C. Simplified analysis and suppression of polarization aberration in planar symmetric optical systems. *Opt. Express* **2023**, *31*, 30750–30766. [CrossRef] [PubMed]
8. Luo, J.; Xu, T.; You, C.; Liu, Y.; Li, C.; Zhang, X.; Dong, J. Design of low polarization off-axis three-mirror reflective optical systems based on deep learning. *Opt. Express* **2023**, *31*, 34477–34493. [CrossRef] [PubMed]
9. Li, Z.; Wu, Q.; Fan, J.; Chen, B.; Liu, X. Polarization Characteristics of Sparse Aperture Optical Imaging Systems. *Acta Opt. Sin.* **2024**, *44*, 1911004.
10. Li, Y.; Yu, W.; Wang, C.; Wang, K.-K.; Liu, J.; Wang, Q.; Liu, Z. Optical system design and polarization aberration compensation based on vector diffraction. *Chin. Opt.* **2025**, *18*, 839–849. [CrossRef]
11. McGuire, J.P.; Chipman, R.A. Diffraction image formation in optical systems with polarization aberrations. I. Formulation and example. *J. Opt. Soc. Am. A* **1990**, *7*, 1614–1626. [CrossRef]
12. Kingma, D.P.; Ba, J. Adam: A method for stochastic optimization. In *Proceedings of the International Conference on Learning Representations*; ICLR: San Diego, CA, USA, 2015.

13. Paszke, A.; Gross, S.; Massa, F.; Lerer, A.; Bradbury, J.; Chanan, G.; Killen, T.; Lin, Z.; Gimelshein, N.; Antiga, L.; et al. PyTorch: An imperative style, high-performance deep learning library. In *Advances in Neural Information Processing Systems 32*; Curran Associates, Inc.: Red Hook, NY, USA, 2019; pp. 8024–8035.
14. Pascanu, R.; Mikolov, T.; Bengio, Y. On the difficulty of training recurrent neural networks. In *Proceedings of the 30th International Conference on Machine Learning*; PMLR: Atlanta, GA, USA, 2013; Volume 28, pp. 1310–1318.

**Disclaimer/Publisher's Note:** The statements, opinions and data contained in all publications are solely those of the individual author(s) and contributor(s) and not of MDPI and/or the editor(s). MDPI and/or the editor(s) disclaim responsibility for any injury to people or property resulting from any ideas, methods, instructions or products referred to in the content.